

# PFAS-Free Locally Concentrated Ionic Liquid Electrolytes for Lithium Metal Batteries

Xu Liu, Alessandro Mariani, Thomas Diemant, Maria Enrica Di Pietro, Xu Dong, Po-Hua Su, Andrea Mele, and Stefano Passerini\*



Cite This: *ACS Energy Lett.* 2024, 9, 3049–3057



Read Online

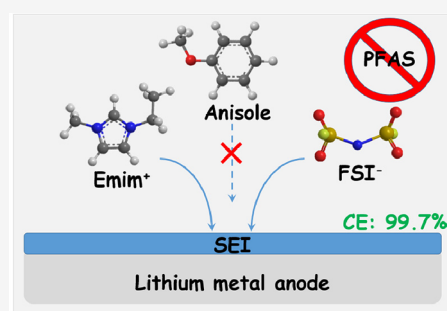
ACCESS |

Metrics & More

Article Recommendations

Supporting Information

**ABSTRACT:** Locally concentrated electrolytes are promising candidates for highly reversible lithium–metal anodes (LMAs) but heavily rely on cosolvents containing  $-\text{CF}_3$  and/or  $-\text{CF}_2-$  groups. The use of these hazardous per- and polyfluoroalkyl substances (PFAS) leads to environmental and occupational safety concerns. Herein, ionic liquids and anisole are employed as solvents and cosolvent, respectively, to construct PFAS-free locally concentrated electrolytes. Anisole not only promotes the ion transport of the electrolytes via inducing a nanophase-segregation solution structure but also modulates the solid electrolyte interphase by affecting the deposition of organic cations and anions on LMAs as well as the conversion of anions to LiF. Optimizing the anisole content enables Li plating/stripping Coulombic efficiency up to 99.71% from 99.19% achieved with the anisole-free ionic liquid electrolyte. As a result, Li/LiFePO<sub>4</sub> and Li/sulfurized-polyacrylonitrile cells employing such an electrolyte and 1.5-fold lithium metal excess achieve stable cycling for 400 and 350 cycles, respectively, with 90% capacity retention.



Lithium metal batteries (LMBs), employing the high-specific-capacity and low-potential lithium metal anode (LMA), are promising candidates for the next generation of high-energy-density secondary batteries.<sup>1</sup> However, the lack of a sufficiently protective solid electrolyte interphase (SEI) on LMAs usually leads to low lithium stripping/plating Coulombic efficiency (CE) and dendritic lithium growth. These limit the cyclic stability of practical LMBs with low negative to positive areal capacity (N/P) ratios.<sup>2</sup>

Since electrolytes play an essential role in the SEI formation, electrolyte engineering has received ever-increasing attention to strengthen the SEI.<sup>3,4</sup> Among the emerging electrolyte concepts to achieve stable, dendrite-free LMAs,<sup>5–10</sup> locally concentrated electrolytes (LCEs) made up of concentrated electrolytes and nonsolvating, low-viscosity cosolvents stand out due to their high lithium stripping/plating CEs.<sup>11–13</sup> Most of the nonsolvating cosolvents presently used in LCEs are highly fluorinated.<sup>11,12,14,15</sup> The fluorinated groups with a strong electron-withdrawing effect decrease the electron density of the coordination moiety, e.g., ether groups, directing the cosolvents to a nonsolvating character and high electrochemical stability against LMAs.<sup>15–17</sup> Some of the fluorinated cosolvents can undergo defluorination, which increases the LiF content in SEIs, further promoting the interfacial stability of LMAs.<sup>12,18,19</sup> On the other hand, the use of these highly fluorinated cosolvents leads to concerns with regard to

environmental and occupational safety issues due to the hazards of the contained  $-\text{CF}_3$  and/or  $-\text{CF}_2-$  groups, i.e., per- and polyfluoroalkyl substances (PFAS), also nicknamed “forever chemicals”.<sup>20,21</sup> In fact, restrictions on the use of PFAS are now being considered worldwide.

Moon et al. recently proposed a few nonfluorinated cosolvents with resonance structure for LCEs, e.g., anisole.<sup>22</sup> The electron pair on the oxygen atom, i.e., the coordinating moiety, is delocalized through the resonance effect of these aromatic cosolvents, which endows the cosolvents with nonsolvating character. Despite the successful development of LCEs with these new cosolvents, the reversibility of LMAs is unfortunately far from being sufficient for more practical use and needs to be further improved. For instance, the CE of LMAs in 3 M lithium bis(fluorosulfonyl)imide (LiFSI) in a mixture of dimethoxyethane (DME) solvent and anisole cosolvent in a volume ratio of 1:2 only reaches 98.5%,<sup>22</sup> while CEs higher than 99.5% are commonly reported with LCEs based on the same salt and solvent when fluorinated cosolvents are employed.<sup>12,23,24</sup>

Received: March 21, 2024

Revised: May 7, 2024

Accepted: May 14, 2024

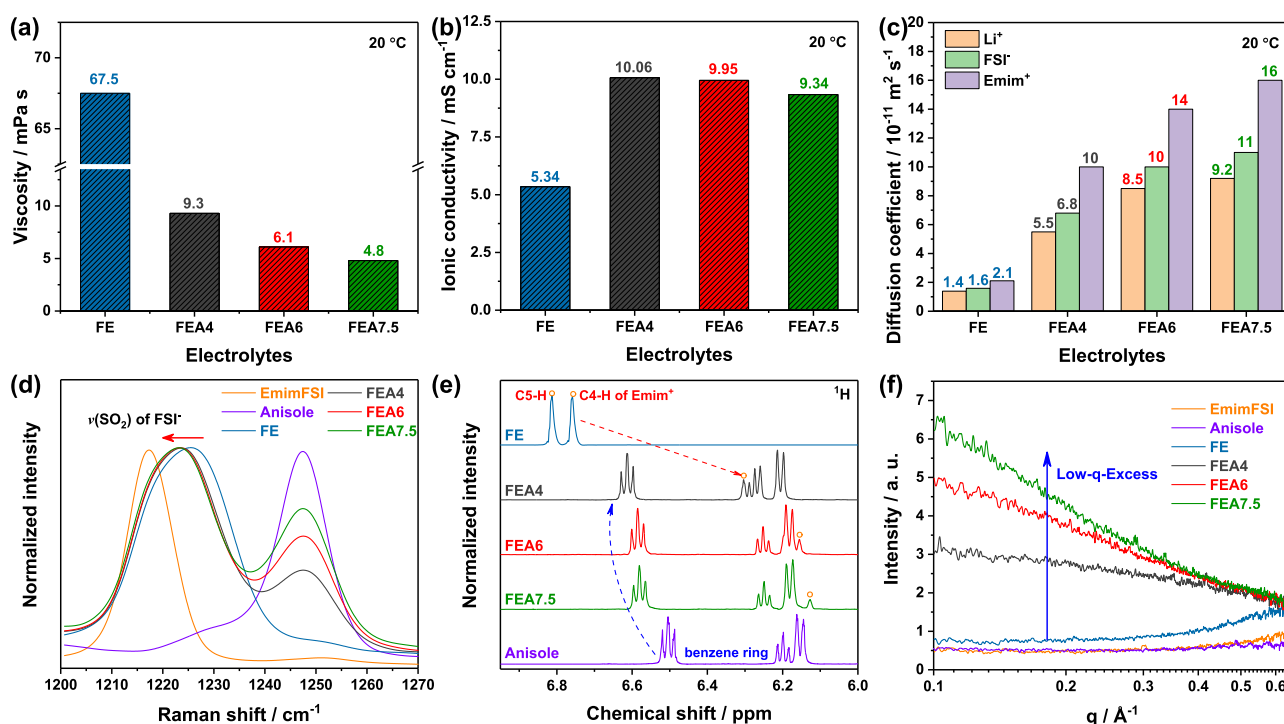


**Figure 1.** Physical properties, solvation, and structure characterization of the electrolytes. (a) Viscosity and (b) ionic conductivity at 20 °C. (c) Self-diffusion coefficients of ions in the electrolytes measured via PFG-NMR at 20 °C. (d) Raman spectra, (e)  $^1\text{H}$  NMR spectra, and (f) SAXS patterns in the  $q$  range of 0.10–0.65  $\text{\AA}^{-1}$  of the electrolytes and corresponding solvents.

In addition to conventional organic solvents, room-temperature ionic liquids can also be used as solvents for LCEs, i.e., locally concentrated ionic liquid electrolytes (LCILEs).<sup>25–27</sup> Herein, an ionic liquid electrolyte (ILE) consisting of LiFSI and EmimFSI (Emim: 1-ethyl-3-methylimidazolium) in a molar ratio of 1:2, i.e.,  $[\text{LiFSI}]_1[\text{EmimFSI}]_2$  (FE), is employed together with anisole to form PFAS-free LCILEs ( $[\text{LiFSI}]_1[\text{EmimFSI}]_2[\text{Anisole}]_x$ ; namely, FEA $x$ ) for highly stable LMBs. To the best of our knowledge, PFAS-free LCILEs employing nonfluorinated, nonsolvating cosolvents for highly reversible LMAs have not been explored yet. The chemical sketches of the electrolyte components are shown in Figure S1.

## PHYSICAL PROPERTIES

To reveal the role played by anisole, FE and three LCILEs with different contents of anisole, namely, FEA4, FEA6, and FEA7.5, were investigated. With an increasing amount of anisole, the concentration of the ionic components decreased (Table S1 and Figure S2a). Since FSI $^-$  is the only fluorine source, it also decreased the fluorine content in the electrolytes (Figure S2b); e.g., the fluorine concentrations were 12.13 and 5.28 mol L $^{-1}$  for FE and FEA6, respectively. This latter value is lower than that in the 1 mol L $^{-1}$  lithium hexafluorophosphate used in commercial lithium-ion batteries and in most LCEs designed for highly reversible LMAs (Table S2). Additionally, the dilution decreased the mass fraction of LiFSI and EmimFSI in the electrolytes (Table S1), which together with the low cost of anisole (Table S3) makes these LCILEs more cost-effective than neat ILEs (Supplementary Discussion 1).

Figure 1a,b displays the viscosity and ionic conductivity of the electrolytes at 20 °C, respectively. Benefiting from the low viscosity of anisole (0.91 mPa s),<sup>28</sup> the viscosity of FE, 67.5 mPa s, is reduced to 6.1 mPa s for FEA6 (Figure 1a). Compared with FE, FEA4 exhibited a much higher ionic

conductivity (10.06 vs 5.34 mS cm $^{-1}$ ). However, the electrolytes with the highest anisole contents showed lower ionic conductivities, resulting from the decreased number of charge carriers (Table S1 and Figure S2a). Even so, the ionic conductivities of FEA6 (9.95 mS cm $^{-1}$ ) and FEA7.5 (9.34 mS cm $^{-1}$ ) are still higher than that of FE.

The self-diffusion coefficients of the ions (Figure 1c) and anisole (Figure S3) in the electrolytes were measured with pulsed field gradient (PFG) NMR. In general, the mobility of the species in the electrolytes follows the trend of viscosity shown in Figure 1a. The dilution leads to improved self-diffusion coefficients of all of the ions. Based on the measured self-diffusion coefficients, the apparent Li $^+$  transference numbers of FE, FEA4, FEA6, and FEA7.5 were calculated to be 0.13, 0.12, 0.13, and 0.12 (see Characterization in the Supporting Information), respectively. These results demonstrate the promoted Li $^+$  mobility upon the dilution. Despite the rather close values, a more pronounced mobility enhancement of FSI $^-$  and, particularly, Emim $^+$  with respect to Li $^+$  is observed (Figure S4), implying a modified coordination of the ions after adding anisole.

## SOLVATION AND SOLUTION STRUCTURE

Figure 1d shows the Raman spectra of EmimFSI, anisole, and the FEA $x$  electrolytes in the region where the  $\nu(\text{SO}_2)$  peak of FSI $^-$  occurs.<sup>29</sup> Weakly interacting with Emim $^+$ , the “free” FSI $^-$  in EmimFSI shows a peak at 1217.3 cm $^{-1}$ . The peak shifts to 1225.5 cm $^{-1}$  in the FE, resulting from the coordination of FSI $^-$  with Li $^+$ . Although neat anisole shows a main peak at 1247.4 cm $^{-1}$  and a weak shoulder at around 1230 cm $^{-1}$ , the FSI $^-$  peak still exhibits a distinguishable shift to lower wavenumbers, indicating a preserved but weakened coordination of FSI $^-$  with Li $^+$ . Also, the shift increases with increasing anisole concentration in the electrolyte, indicating that the portion

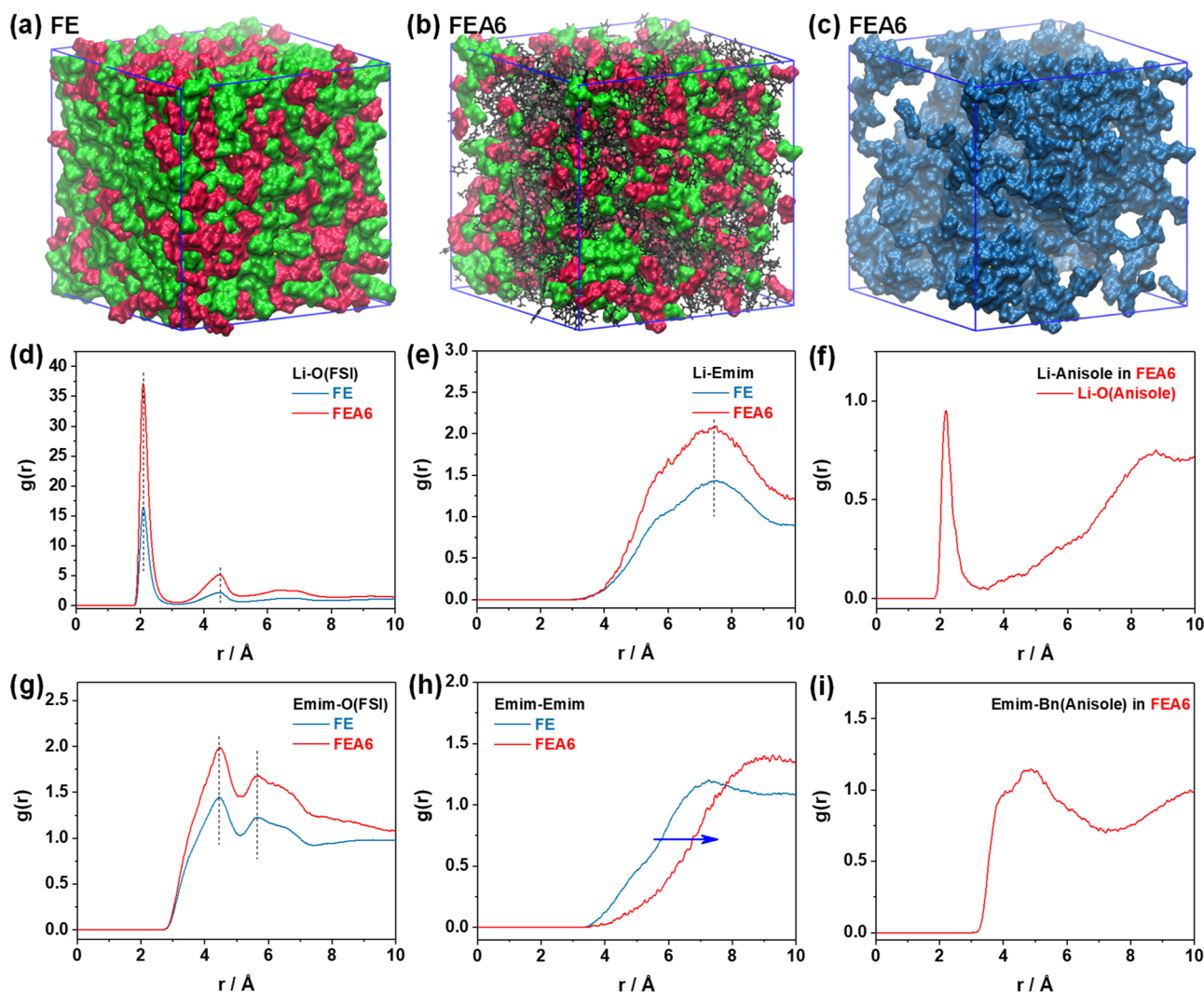


**Figure 2.** MD simulations for FE and FEA6. Snapshots of the MD simulated boxes of (a) FE and (b,c) FEA6. In (a) and (b), Emim<sup>+</sup>, FSI<sup>-</sup>, Li<sup>+</sup>, and anisole are represented by red, green, yellow, and black surfaces, respectively. In (c), anisole is invisible, while the blue surface represents Emim<sup>+</sup>/FSI<sup>-</sup>. RDFs of (d) Li-O(FSI), (e) Li-Emim, (f) Li-O(Anisole), (g) Emim-O(FSI), (h) Emim-Emim, and (i) Emim-Bn(Anisole) in FE and FEA6. O and Bn represent the oxygen atom and benzene ring, respectively. For Emim<sup>+</sup> and the benzene ring, the geometric center of the ring is used for the calculation of RDFs.

of FSI<sup>-</sup> coordinating with Li<sup>+</sup> is slightly affected by the cosolvent content. Nevertheless, this shift is rather small with respect to that generated by strongly solvating cosolvents, e.g., dimethyl carbonate,<sup>30</sup> which is consistent with the reported poor coordination ability of anisole toward Li<sup>+</sup>.<sup>22</sup>

The <sup>1</sup>H NMR spectra of anisole and the electrolytes were subsequently compared (Figure 1e). The peaks at 6.82 and 6.76 ppm in the spectrum of FE are assigned to the C5-H and C4-H atoms of Emim<sup>+</sup>, respectively, as illustrated in Figure S5a. Upon addition of anisole, the C5-H and C4-H peaks showed an upfield shift to a lower frequency, which becomes more pronounced with increasing concentrations of anisole. A similar development is also observed for the C2-H peak of Emim<sup>+</sup> (Figure S5b). These results verify the change of the Emim<sup>+</sup> coordination environment. Regarding anisole, three signals from the protons of its benzene ring were observed. The chemical shift of anisole's peaks exhibits an upfield shift with its content, which implies an interaction between anisole and the FE species.

The wide- and small-angle X-ray scattering (W/SAXS) tests with a  $q$  range of 0.4–2.0 Å<sup>-1</sup> revealed much higher intensities for the LCILEs in the  $q$  range below 0.6 Å<sup>-1</sup> with respect to the FE, EmimFSI, and anisole (Figure S6). The SAXS patterns focusing on the low- $q$  range (0.1–0.65 Å<sup>-1</sup>) are shown in Figure 1f. EmimFSI, anisole, and FE exhibited flat SAXS patterns at  $q$  lower than 0.3 Å<sup>-1</sup>, which means that they are homogeneous at scales larger than ~20 Å.<sup>31</sup> However, the scattered intensity at the low  $q$  values diverges as the amount of anisole is increased in LCILEs, reflecting the heterogeneity on a nanometric scale. Most notably, the overall signal of the LCILEs is more intense than the sum of the scattered intensity of the starting materials, i.e., anisole and FE. These features are known as Low- $q$ -Excess (LqE)<sup>32–34</sup> and are the fingerprint of phase nanosegregation,<sup>35</sup> meaning that the constituent phases of a macroscopically homogeneous mixture are separated at the nanoscale.

To resolve the effect of anisole on the local heterogeneity and the interactions between ions and cosolvent molecules, molecular dynamic (MD) simulations of FE and FEA6 were

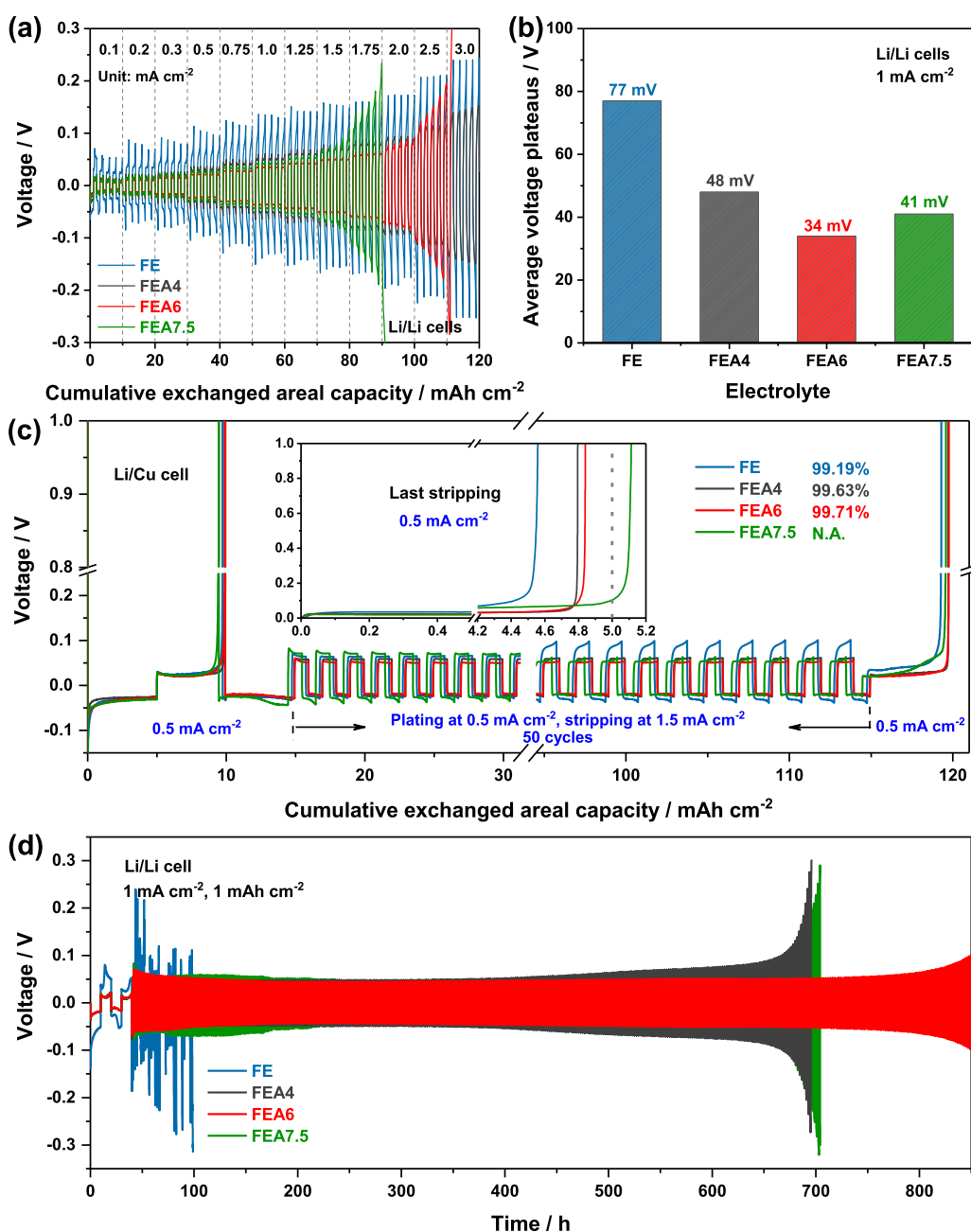


Figure 3. Electrochemical performance of LMAs in the electrolytes. (a) Voltage profiles of Li/Li cells at various current densities. The areal capacity for each cycle was 1 mAh cm<sup>-2</sup>. (b) Average charge voltage of Li/Li cells at 1 mA cm<sup>-2</sup>. (c) Voltage profiles of Li/Cu cells for CE tests of lithium stripping/plating. (d) Voltage profiles of Li/Li cells upon prolonged cycling at 1 mA cm<sup>-2</sup> after two formation cycles at 0.1 mA cm<sup>-2</sup>. The areal capacity for each cycle was 1 mAh cm<sup>-2</sup>.

conducted. Figure 2a,b shows snapshots of the simulation boxes of FE and FEA6, respectively. As observed, the ions glue together, forming ionic nanodomains where Li<sup>+</sup> is surrounded by anions, while anisole tends to form separate regions. The absence of ions, particularly Li<sup>+</sup>, in the cosolvent nanodomains is visualized in Figure 2c, where anisole molecules are removed. The pronounced nanoscale heterogeneity of FEA6 explains the characteristic LqE observed in the SAXS patterns of the LCILEs (Figure 2f).

To clarify the local solvation in more detail, we employed radial distribution functions (RDFs). Since the volume fraction occupied by the ions is smaller in FEA6 than in FE, the intensity of the curves for FEA6 is higher than that for FE.

Figure 2d,e shows the coordination of Li<sup>+</sup> by oxygen atoms from FSI<sup>-</sup> (O(FSI<sup>-</sup>)) and the Emim<sup>+</sup> ring, respectively. Since Li<sup>+</sup> coordinates to FSI<sup>-</sup> rather than Emim<sup>+</sup>, sharp peaks at 2.10 Å are observed in the Li-O(FSI) curves, while the Li-Emim curves show a negligible intensity in the region below 3.0 Å. These features do not change in the presence of anisole. The peak located at 2.18 Å in the RDF of Li<sup>+</sup> coordinated by the oxygen atom of anisole in FEA6 (Figure 2f) indicates the presence of anisole in the first solvation shell of Li<sup>+</sup>. In a further step, the discrete coordination numbers of the FSI<sup>-</sup> and anisole oxygen atoms toward Li<sup>+</sup> in the electrolytes were calculated (Figure S7). The Li<sup>+</sup> average coordination number by FSI<sup>-</sup> oxygens decreases slightly from 4.925 in FE to 4.590 in FEA6,

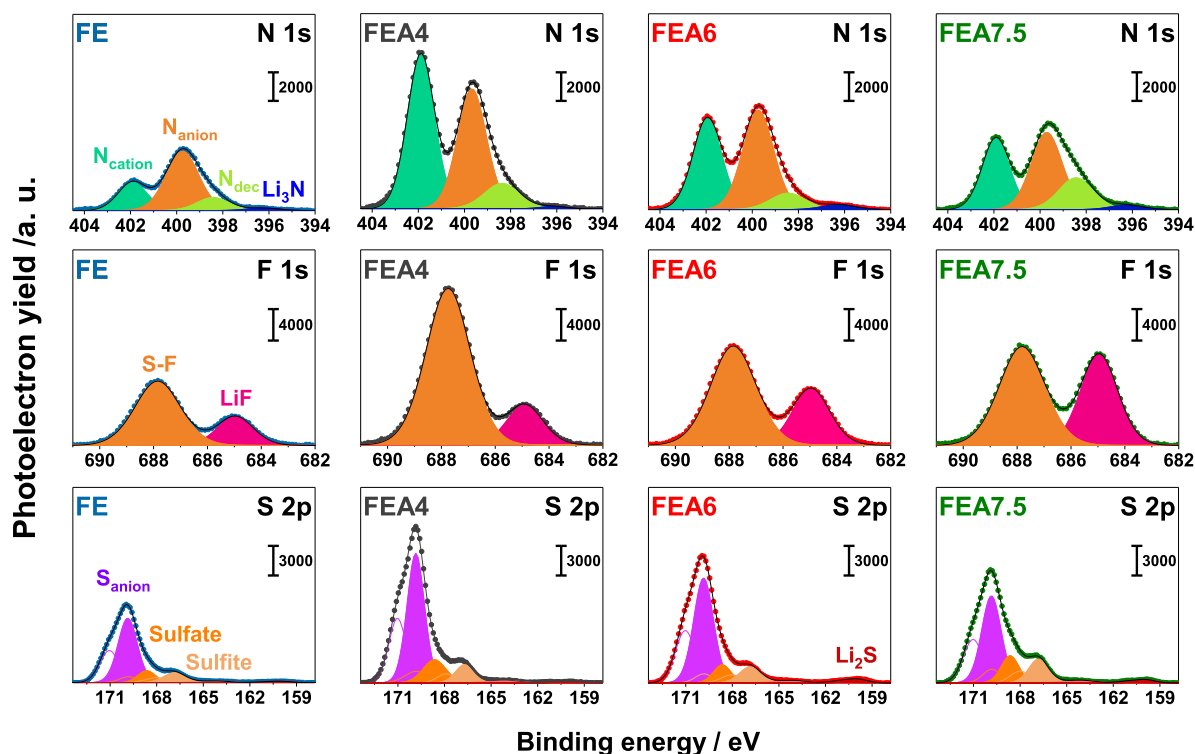


Figure 4. XPS characterization of the SEI on the surface of lithium deposited on Cu. N 1s, F 1s, and S 2p XPS detail spectra after background subtraction from samples with  $3.0 \text{ mAh cm}^{-2}$  lithium deposited on Cu in FE, FEA4, FEA6, and FEA7.5 at  $0.5 \text{ mA cm}^{-2}$ .

which matches the shift of the  $\nu(\text{SO}_2)$  peak in Figure 1d. For anisole, only  $\sim 10\%$  of  $\text{Li}^+$  interacts with a single methoxy group and the average coordination number is only 0.09 (Figure S7c). These results confirm the generally weak coordination between  $\text{Li}^+$  and anisole, as well as its limited effect on the FSI<sup>-</sup>-dominating solvation of  $\text{Li}^+$ .

Figure 2g–i shows the RDFs of Emim-O(FSI), Emim-Emim, and Emim-Anisole in the electrolytes, respectively. The position of the peaks in the Emim-O(FSI) curve is not changed by anisole (Figure 2g), but the feature reflecting  $\pi$ – $\pi$  stacking of Emim<sup>+</sup> shows a significant shift (Figure 2h). Specifically, one peak and a shoulder are observed at  $\sim 6$  and  $5 \text{ \AA}$ , respectively, for FE. However, the peak shifts to larger values ( $>8 \text{ \AA}$ ) in FEA6, indicating for Emim<sup>+</sup> interaction with other species. Meanwhile, a peak at  $\sim 5.3 \text{ \AA}$  and a well-defined shoulder at  $\sim 4 \text{ \AA}$  are observed in the Emim-Anisole correlation (Figure 2i), which together with the above observation is compatible with an Emim-Anisole-Emim alternated  $\pi^+ - \pi - \pi^+$  stacking. Its occurrence is more clearly visualized with the spatial distribution functions of Emim<sup>+</sup> in FE and FEA6 (Figure S8). This interaction also explains the peak shift in the  $^1\text{H}$  NMR spectra (Figure 1e).

These results demonstrate that FEA6 is a typical LCE exhibiting a local heterogeneous solution structure, resulting from the well-balanced interaction between anisole and the ions (Supplementary Discussion 2). Due to the generally poor affinity between anisole and  $\text{Li}^+$ , as well as other ions, separated nanodomains are formed, which helps to preserve the local coordination of the ions in their parental solutions upon dilution. Meanwhile, interactions between anisole and ions still occur at the boundary of the nanodomains, which prevents the macroscopic phase separation and influences the local solvation and the ions' transport (Supplementary Discussion 3).

## ELECTROCHEMICAL PERFORMANCE AND INTERFACIAL CHEMISTRY OF LMAS

Figure 3a shows the rate capabilities of Li/Li cells. The use of FE or FEA4 enabled the cells to operate at up to  $3.0 \text{ mA cm}^{-2}$ . When FEA6 and FEA7.5 were employed, the cells were terminated due to the cell voltage reaching the cutoff ( $0.3 \text{ V}$ ) already at  $2.5$  and  $1.75 \text{ mA cm}^{-2}$ , respectively. This behavior can be attributed to insufficient  $\text{Li}^+$  transport at elevated current densities. Considering the limited influence of anisole on the transference number of  $\text{Li}^+$ , but its significant promotion on the  $\text{Li}^+$  self-diffusion coefficient, the operative current density decrease for LCILEs with high anisole contents can be assigned to the reduced  $\text{Li}^+$  concentration. Nonetheless, all of the LCILEs led to decreased cell overvoltage with respect to FE at lower current densities, particularly FEA6 (Figure S9). Specifically, the average voltages of Li/Li cells upon charge at  $1 \text{ mA cm}^{-2}$  were  $77$ ,  $48$ ,  $34$ , and  $41 \text{ mV}$  employing FE, FEA4, FEA6, and FEA7.5, respectively (Figure 3b). Although Li/FE/Li survived from the operation at higher current densities, the relatively high voltage reached ( $210 \text{ mV}$ ) at  $2.5 \text{ mA cm}^{-2}$  excludes its practical use. Clearly, the LCILEs offer improved kinetics in comparison to neat ILE (FE) in terms of lithium stripping/plating.

Figure 3c displays the voltage profiles upon the Li plating–stripping cycles performed to evaluate the CE of the electrolytes. After the initial formation cycle, FE showed a CE of  $99.2\%$ . However, FEA4 and FEA6 granted improved CEs,  $99.6\%$  and  $99.7\%$ , respectively, indicating reduced interfacial side reactions and promoted reversibility of LMAs. To confirm these results, the CE test for FEA6 was reproduced in two experiments (Figure S10). It is worth mentioning that the CE of FEA6 is superior to that granted by most LCEs even employing fluorinated cosolvents and/or ionic liquid solvents,

approaching the state-of-the-art value (see Table S2). Particularly, the CE achieved using 3 M LiFSI in DME/anisole (1:2 vol) is only 98.5%,<sup>22</sup> reflecting the advantage of IL as solvent for LCEs with nonfluorinated cosolvents. When FEA7.5 was employed as the electrolyte, the CE was not available due to the presence of a soft short circuit (Supplementary Discussion 4). These results demonstrate that FEA6 has the optimal composition granting high reversibility of LMAs, which is also supported by the cycling performance of symmetrical Li/Li cells (Figure 3d) and the morphology of deposited Li on Cu (Figure S11) and cycled Li foils with different electrolytes (Figure S12).

The SEIs on the Li surface formed in the FE and the LCILEs were characterized using X-ray photoelectron spectroscopy (XPS). The results in the N 1s, F 1s, and S 2p regions are shown in Figure 4, while the C 1s and O 1s regions are displayed in Figure S13. The details of the binding energy and assignment of the peaks observed in Figure 4 are provided in Table 1.

**Table 1. Assignment of the XPS Peaks Observed in Figure 4**

signal	position/ eV	abbreviation	assignment	ref
N 1s	401.9	N <sub>cation</sub>	deposited Emim <sup>+</sup>	36–38
	399.7	N <sub>anion</sub>	deposited FSI <sup>-</sup>	
	398.4	N <sub>dec</sub>	partially decomposed Emim <sup>+</sup> and FSI <sup>-</sup>	
	396.2	Li <sub>3</sub> N	Li <sub>3</sub> N generated from Emim <sup>+</sup> and FSI <sup>-</sup>	
F 1s	687.8	S–F	S–F bond from FSI <sup>-</sup> and its derivatives	39
	685.0	LiF	LiF generated from FSI <sup>-</sup>	
S 2p <sub>3/2</sub>	169.9	S <sub>anion</sub>	deposited FSI <sup>-</sup>	40, 41
	168.6	sulfate	sulfates derived from FSI <sup>-</sup>	
	166.8	sulfite	sulfites derived from FSI <sup>-</sup>	
	160.0	Li <sub>2</sub> S	Li <sub>2</sub> S derived from FSI <sup>-</sup>	

Clearly, the SEI generated in the FE is derived from both Emim<sup>+</sup> and FSI<sup>-</sup>. The same species were also observed in the SEIs formed with LCILEs, but their concentration showed a strong dependence on the anisole content in the electrolyte. With increasing anisole contents, the intensity of several peaks associated with the deposition of Emim<sup>+</sup> and FSI<sup>-</sup> exhibited a bell-shaped evolution, reaching the highest intensity for the FEA4 sample, e.g., N<sub>cation</sub> (N 1s), N<sub>anion</sub> (N 1s), S–F (F 1s), and S<sub>anion</sub> (S 2p). This trend matches with the ionic conductivity of the electrolytes, implying a correlation between the SEI formation and the IL ions' transport, which is a trade-off of ion concentration (Figure S2a) and ion mobility (Figure 1c). The correlation resides in the SEI formation being accompanied by the consumption of the ions at the electrolyte/electrode interface, which relies on their transport from the bulk electrolyte to the electrode interface. Considering the XPS results and LMA reversibility of FE and FEA4, one can conclude that the promoted deposition of Emim<sup>+</sup> and FSI<sup>-</sup> is generally beneficial for a more protective SEI.<sup>27</sup> On the other hand, the reduced deposition of pristine FSI<sup>-</sup> is accompanied by its more pronounced reduction, as indicated by the higher intensity of the LiF peak (see F 1s spectra) in the electrolytes with larger anisole contents. Such a larger decomposition of FSI<sup>-</sup> (to form LiF) can be considered as a consequence of the insufficient supply of ions at the

electrode/electrolyte interface. It has been demonstrated that LiF is an electronic insulator but a Li<sup>+</sup> conductor with high mechanical strength and, due to that, it is a desired component for highly protective SEIs granting reversibility to LMAs.<sup>9,42</sup> One can infer that these two opposite effects arising from increasing anisole contents control the reversibility of LMAs. In FEA6, these two effects are well balanced, leading to the best compatibility toward LMAs, which effectively suppressed their side reactions, e.g., those involving anisole. In fact, a contribution from anisole to the SEI was traced in the SEI formed with FEA7.5 via its C 1s and O 1s spectra (Figure S13), indicating that the SEI does not prevent the decomposition of anisole.

## ■ PERFORMANCE OF LI/LFP AND LI/SPAN CELLS

Following the results presented above, FEA6 was selected for the evaluation of LMBs. The linear sweep voltammograms using carbon black coated Al foil as the working electrode indicated an anodic stability up to 3.9 V vs Li/Li<sup>+</sup> (Figure S14), which is inferior to that of FE (up to 4.5 V vs Li/Li<sup>+</sup>) but still sufficient for LFP cathodes.

Figure 5a shows the cycling performance of an exemplary Li/LFP cell with 500 μm thick LMA, a 10 mg cm<sup>-2</sup> LFP cathode, and 75 μL of electrolyte. The voltage profiles are shown in Figure 5b for FEA6 and in Figure S15 for FE. After the formation cycles at C/10 (1C = 160 mA g<sup>-1</sup>), 135 and 140 mAh g<sup>-1</sup> were delivered with FE and FEA6, respectively. The higher specific capacity obtained with FEA6 can be attributed to a synergistic effect of its superior Li<sup>+</sup> transport, Li stripping/plating kinetics, and fluidity. In the following cycles (C/3 charge and 1C discharge), the specific capacity with FE slightly increased to 142 mAh g<sup>-1</sup> at the 35th cycle followed by rapid fading from the 75th cycle, reaching a capacity retention of 90% at the 79th cycle. Due to the intrinsic high cyclability of LFP, this poor performance can be unambiguously attributed to the insufficient reversibility of LMAs in FE. By contrast, the FEA6-based cell experienced a gradual capacity increase to 152 mAh g<sup>-1</sup> at the 400th cycle, showing no capacity fading.

In a further step, cells with a thinner LMA (2.25 mAh cm<sup>-2</sup>, N/P ratio of 1.5) and lower electrolyte amount (20 μL/cell) were tested with the same protocol. Figure 5c shows the discharge specific capacities and CEs for both electrolytes (FE and FEA6). The discharge/charge profiles are shown in Figure 5d for FEA6 and Figure S16 for FE. The decreased N/P ratio did not affect the discharge capacity in the initial cycles, but a rapid capacity fading of the FE-based cell was observed from the 27th cycle, while the 90% capacity retention was hit after 54 cycles. In contrast, benefiting from the high reversibility of LMAs in FEA6, the Li/FEA6/LFP cell exhibited a remarkable capacity retention of 94% at the 400th cycle. A similar capacity retention of 92% was obtained in a duplicate experiment (Figure S17).

In addition to LFP, the compatibility of the LCILE with SPAN cathodes, exhibiting a reversible capacity up to 600 mAh g<sup>-1</sup>, was tested.<sup>43</sup> Benefiting from the cathode electrolyte interphase (CEI) derived from Emim<sup>+</sup> and FSI<sup>-</sup> (Figure S18), SPAN cathodes (2.8 mg cm<sup>-2</sup>) paired with 500 μm thick LMAs exhibited a capacity retention of 98% after 400 cycles in FEA6 (Figure S19).<sup>44</sup> Then, cells with a 2.8 mg cm<sup>-2</sup> SPAN cathode, 3.75 mAh cm<sup>-2</sup> LMA, and 20 μL of electrolyte were tested. Figure 5e shows the discharge specific capacities and CE in both electrolytes (FE and FEA6). The discharge/charge profiles are shown in Figure 5f for FEA6 and Figure S20 for

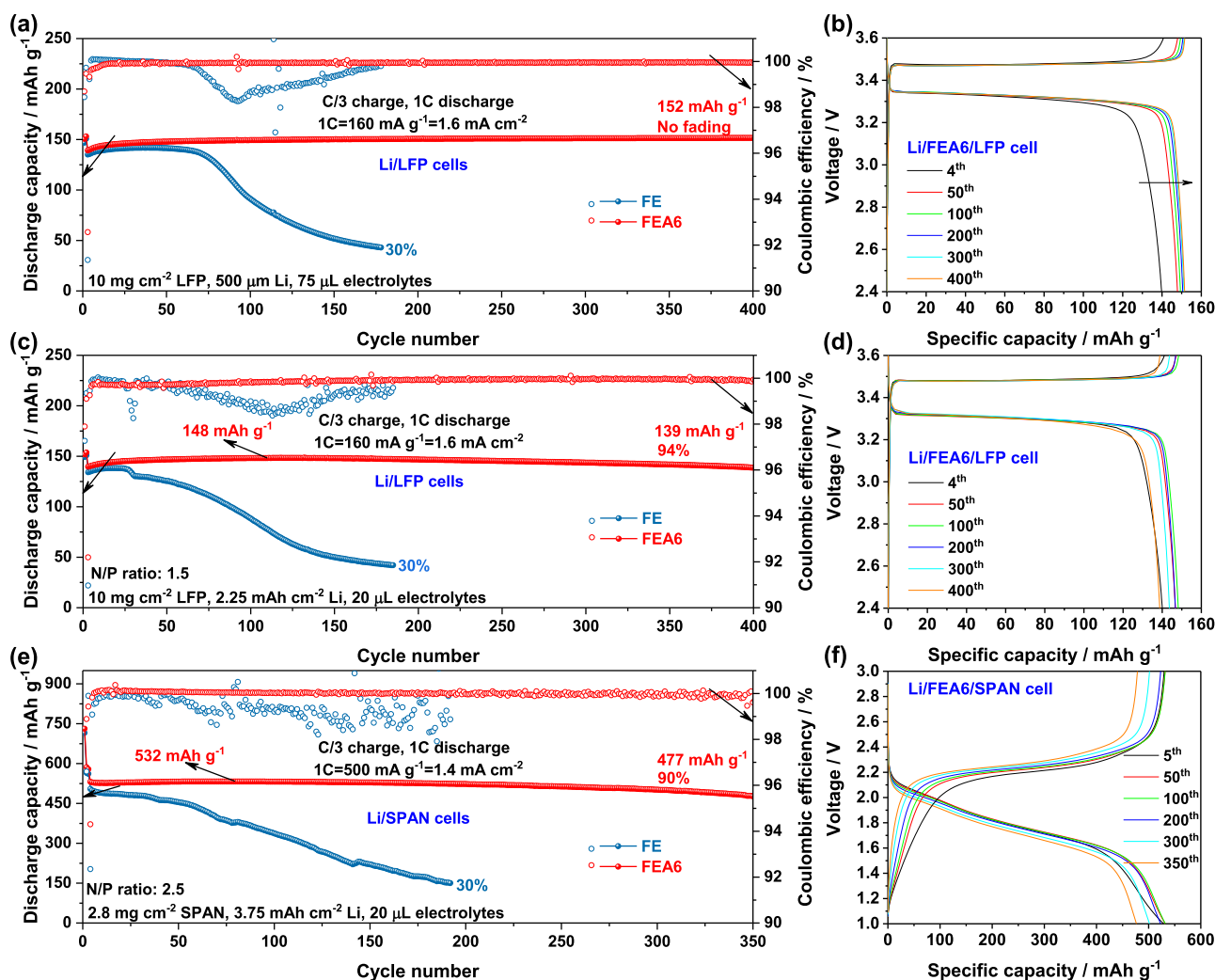


Figure 5. Performance of Li/LFP and Li/SPAN cells with FE or FEA6 as the electrolyte. (a) Cycling performance and (b) voltage profiles of cells with  $10 \text{ mg cm}^{-2}$  LFP cathode,  $500 \mu\text{m}$  thick LMA, and  $75 \mu\text{L}$ /cell electrolyte. (c) Cycling performance and (d) voltage profiles of cells with  $10 \text{ mg cm}^{-2}$  LFP cathode,  $2.25 \text{ mAh cm}^{-2}$  LMA, and  $20 \mu\text{L}$ /cell electrolyte. The Li/LFP cells were charged at C/3 and discharged at 1C after two formation cycles at C/10 between 2.4 and 3.6 V, where  $1\text{C} = 160 \text{ mA g}^{-1} = 1.6 \text{ mA cm}^{-2}$ . (e) Cycling performance and (f) voltage profiles of cells with  $2.8 \text{ mg cm}^{-2}$  SPAN cathode,  $3.75 \text{ mAh cm}^{-2}$  LMA, and  $20 \mu\text{L}$ /cell electrolyte. The Li/SPAN cells were charged at C/3 and discharged at 1C after three formation cycles at C/10 between 1.0 and 3.0 V, where  $1\text{C} = 500 \text{ mA g}^{-1} = 1.4 \text{ mA cm}^{-2}$ .

FE. Compared with FE, FEA6 led to higher reversible specific discharge capacities ( $529$  vs  $499 \text{ mAh g}^{-1}$  at the fifth cycle) and capacity retention. The FE-based cell exhibited a fast capacity fading, reaching a capacity retention of 90% at the 54th cycle; while the FEA6-based cell delivered  $477 \text{ mA g}^{-1}$  at the 350th cycle, exhibiting a capacity retention of 90%. A similar capacity retention of 87% was obtained in a parallel experiment (Figure S21).

In summary, PFAS-free LCILEs employing anisole as nonfluorinated cosolvent have been developed, enabling LMAs with high CEs and highly stable cycling of Li/LFP and Li/SPAN cells with low Li metal excess. The addition of anisole to FE generates a nanophase segregation in the electrolyte solution, which effectively promotes the  $\text{Li}^+$  transport without degrading the anion-dominated solvation of  $\text{Li}^+$ . Additionally, the content of anisole in the electrolyte modulates the SEI composition by affecting the deposition of organic cations and anions on LMAs, as well as the conversion of the anion to  $\text{LiF}$ .

## ASSOCIATED CONTENT

### Supporting Information

The Supporting Information is available free of charge at <https://pubs.acs.org/doi/10.1021/acseenergylett.4c00814>.

Experimental details, computational Details; Supplementary Discussions 1–4, composition of electrolytes, comparison of fluorine concentration and CE for various reported LCEs, price of the electrolyte components, chemical structure of the electrolyte components, concentration of electrolyte components and fluorine, self-diffusion coefficient of the electrolyte species,  $^1\text{H}$  NMR spectra, WAXS spectra, computed coordination numbers, spatial distribution functions around  $\text{Emim}^+$ , voltage profiles of Li/Li cells at various current densities, duplicate tests of Li/Cu, Li/LFP, and Li/SPAN cells employing FEA6, morphology of deposited Li on Cu and cycled Li, C 1s and O 1s XPS spectra of Li deposited on Cu, anodic stability of FEA6, voltage profiles of Li/LFP and Li/SPAN cells employing FE, and XPS results of SPAN cycled in FEA6 (PDF)

## AUTHOR INFORMATION

## Corresponding Author

**Stefano Passerini** – Helmholtz Institute Ulm (HIU)  
Electrochemical Energy Storage, 89081 Ulm, Germany;  
Karlsruhe Institute of Technology (KIT), 76021 Karlsruhe,  
Germany; Chemistry Department, Sapienza University of  
Rome, 00185 Rome, Italy; [orcid.org/0000-0002-6606-5304](https://orcid.org/0000-0002-6606-5304); Email: [stefano.passerini@kit.edu](mailto:stefano.passerini@kit.edu)

## Authors

**Xu Liu** – Helmholtz Institute Ulm (HIU) Electrochemical  
Energy Storage, 89081 Ulm, Germany; Karlsruhe Institute of  
Technology (KIT), 76021 Karlsruhe, Germany;  
[orcid.org/0000-0003-0532-316X](https://orcid.org/0000-0003-0532-316X)

**Alessandro Mariani** – ELETTRA Sincrotrone Trieste, 34012  
Basovizza, Trieste, Italy; [orcid.org/0000-0002-3686-2169](https://orcid.org/0000-0002-3686-2169)

**Thomas Diemant** – Helmholtz Institute Ulm (HIU)  
Electrochemical Energy Storage, 89081 Ulm, Germany;  
Karlsruhe Institute of Technology (KIT), 76021 Karlsruhe,  
Germany

**Maria Enrica Di Pietro** – Department of Chemistry, Materials  
and Chemical Engineering “Giulio Natta”, Politecnico di  
Milano, I-20133 Milan, Italy; [orcid.org/0000-0002-2370-1948](https://orcid.org/0000-0002-2370-1948)

**Xu Dong** – Helmholtz Institute Ulm (HIU) Electrochemical  
Energy Storage, 89081 Ulm, Germany; Karlsruhe Institute of  
Technology (KIT), 76021 Karlsruhe, Germany

**Po-Hua Su** – Helmholtz Institute Ulm (HIU) Electrochemical  
Energy Storage, 89081 Ulm, Germany; Karlsruhe Institute of  
Technology (KIT), 76021 Karlsruhe, Germany

**Andrea Mele** – Department of Chemistry, Materials and  
Chemical Engineering “Giulio Natta”, Politecnico di Milano,  
I-20133 Milan, Italy; [orcid.org/0000-0002-0351-0538](https://orcid.org/0000-0002-0351-0538)

Complete contact information is available at:

<https://pubs.acs.org/10.1021/acseenergylett.4c00814>

## Notes

The authors declare no competing financial interest.

## ACKNOWLEDGMENTS

This work was supported by the China Scholarship Council (CSC) and the Helmholtz Association Basic funding. The postdoctoral fellowship in the framework of the “MSCA EF Master Class 2018” funding programme in the Politecnico di Milano is also acknowledged.

## REFERENCES

- (1) Niu, C.; Liu, D.; Lochala, J. A.; Anderson, C. S.; Cao, X.; Gross, M. E.; Xu, W.; Zhang, J. G.; Whittingham, M. S.; Xiao, J.; et al. Balancing Interfacial Reactions to Achieve Long Cycle Life in High-Energy Lithium Metal Batteries. *Nat. Energy* **2021**, *6* (7), 723–732.
- (2) Xue, W.; Huang, M.; Li, Y.; Zhu, Y. G.; Gao, R.; Xiao, X.; Zhang, W.; Li, S.; Xu, G.; Yu, Y.; et al. Ultra-High-Voltage Ni-Rich Layered Cathodes in Practical Li Metal Batteries Enabled by a Sulfonamide-Based Electrolyte. *Nat. Energy* **2021**, *6* (5), 495–505.
- (3) Zhang, J. G.; Xu, W.; Xiao, J.; Cao, X.; Liu, J. Lithium Metal Anodes with Nonaqueous Electrolytes. *Chem. Rev.* **2020**, *120* (24), 13312–13348.
- (4) Wang, H.; Yu, Z.; Kong, X.; Kim, S. C.; Boyle, D. T.; Qin, J.; Bao, Z.; Cui, Y. Liquid Electrolyte: The Nexus of Practical Lithium Metal Batteries. *Joule* **2022**, *6* (3), 588–616.
- (5) Rustomji, C. S.; Yang, Y.; Kim, T. K.; Mac, J.; Kim, Y. J.; Caldwell, E.; Chung, H.; Meng, Y. S. Liquefied Gas Electrolytes for

Electrochemical Energy Storage Devices. *Science* **2017**, *356* (6345), No. eaal4263.

(6) Kim, S. C.; Wang, J.; Xu, R.; Zhang, P.; Chen, Y.; Huang, Z.; Yang, Y.; Yu, Z.; Oyakhire, S. T.; Zhang, W.; et al. High-Entropy Electrolytes for Practical Lithium Metal Batteries. *Nat. Energy* **2023**, *8* (8), 814–826.

(7) Xia, Y.; Zhou, P.; Kong, X.; Tian, J.; Zhang, W.; Yan, S.; Hou, W.; Zhou, H. Y.; Dong, H.; Chen, X.; et al. Designing an Asymmetric Ether-like Lithium Salt to Enable Fast-Cycling High-Energy Lithium Metal Batteries. *Nat. Energy* **2023**, *8* (9), 934–945.

(8) Yu, Z.; Rudnicki, P. E.; Zhang, Z.; Huang, Z.; Celik, H.; Oyakhire, S. T.; Chen, Y.; Kong, X.; Kim, S. C.; Xiao, X.; et al. Rational Solvent Molecule Tuning for High-Performance Lithium Metal Battery Electrolytes. *Nat. Energy* **2022**, *7* (1), 94–106.

(9) Fan, X.; Chen, L.; Borodin, O.; Ji, X.; Chen, J.; Hou, S.; Deng, T.; Zheng, J.; Yang, C.; Liou, S. C.; et al. Non-Flammable Electrolyte Enables Li-Metal Batteries with Aggressive Cathode Chemistries. *Nat. Nanotechnol.* **2018**, *13* (8), 715–722.

(10) Yamada, Y.; Wang, J.; Ko, S.; Watanabe, E.; Yamada, A. Advances and Issues in Developing Salt-Concentrated Battery Electrolytes. *Nature Energy* **2019**, *4* (4), 269–280.

(11) Ren, X.; Zou, L.; Cao, X.; Engelhard, M. H.; Liu, W.; Burton, S. D.; Lee, H.; Niu, C.; Matthews, B. E.; Zhu, Z.; et al. Enabling High-Voltage Lithium-Metal Batteries under Practical Conditions. *Joule* **2019**, *3* (7), 1662–1676.

(12) Zhu, C.; Sun, C.; Li, R.; Weng, S.; Fan, L.; Wang, X.; Chen, L.; Noked, M.; Fan, X. Anion-Diluent Pairing for Stable High-Energy Li Metal Batteries. *ACS Energy Lett.* **2022**, *7* (4), 1338–1347.

(13) Cao, X.; Jia, H.; Xu, W.; Zhang, J.-G. Review—Localized High-Concentration Electrolytes for Lithium Batteries. *J. Electrochem. Soc.* **2021**, *168* (1), No. 010522.

(14) Wu, Z.; Li, R.; Zhang, S.; lv, L.; Deng, T.; Zhang, H.; Zhang, R.; Liu, J.; Ding, S.; Fan, L.; et al. Deciphering and Modulating Energetics of Solvation Structure Enables Aggressive High-Voltage Chemistry of Li Metal Batteries. *Chem.* **2023**, *9* (3), 650–664.

(15) Chen, S.; Zheng, J.; Yu, L.; Ren, X.; Engelhard, M. H.; Niu, C.; Lee, H.; Xu, W.; Xiao, J.; Liu, J.; et al. High-Efficiency Lithium Metal Batteries with Fire-Retardant Electrolytes. *Joule* **2018**, *2* (8), 1548–1558.

(16) Chen, S.; Zheng, J.; Mei, D.; Han, K. S.; Engelhard, M. H.; Zhao, W.; Xu, W.; Liu, J.; Zhang, J. G. High-Voltage Lithium-Metal Batteries Enabled by Localized High-Concentration Electrolytes. *Adv. Mater.* **2018**, *30* (21), No. 1706102.

(17) Ren, X.; Chen, S.; Lee, H.; Mei, D.; Engelhard, M. H.; Burton, S. D.; Zhao, W.; Zheng, J.; Li, Q.; Ding, M. S.; et al. Localized High-Concentration Sulfone Electrolytes for High-Efficiency Lithium-Metal Batteries. *Chem.* **2018**, *4* (8), 1877–1892.

(18) Yoo, D. J.; Yang, S.; Kim, K. J.; Choi, J. W. Fluorinated Aromatic Diluent for High-Performance Lithium Metal Batteries. *Angew. Chem., Int. Ed.* **2020**, *59* (35), 14869–14876.

(19) Jiang, Z.; Zeng, Z.; Liang, X.; Yang, L.; Hu, W.; Zhang, C.; Han, Z.; Feng, J.; Xie, J. Fluorobenzene, A Low-Density, Economical, and Bifunctional Hydrocarbon Cosolvent for Practical Lithium Metal Batteries. *Adv. Funct. Mater.* **2021**, *31* (1), No. 2005991.

(20) Han, J.; Kiss, L.; Mei, H.; Remete, A. M.; Ponikvar-Svet, M.; Sedgwick, D. M.; Roman, R.; Fustero, S.; Moriwaki, H.; Soloshonok, V. A. Chemical Aspects of Human and Environmental Overload with Fluorine. *Chem. Rev.* **2021**, *121* (8), 4678–4742.

(21) Flerlage, H.; Slootweg, J. C. Modern Chemistry Is Rubbish. *Nat. Rev. Chem.* **2023**, *7* (9), 593–594.

(22) Moon, J.; Kim, D. O.; Bekaert, L.; Song, M.; Chung, J.; Lee, D.; Hubin, A.; Lim, J. Non-Fluorinated Non-Solvating Cosolvent Enabling Superior Performance of Lithium Metal Negative Electrode Battery. *Nat. Commun.* **2022**, *13*, 4538.

(23) Cao, X.; Ren, X.; Zou, L.; Engelhard, M. H.; Huang, W.; Wang, H.; Matthews, B. E.; Lee, H.; Niu, C.; Arey, B. W.; et al. Monolithic Solid–Electrolyte Interphases Formed in Fluorinated Orthoformate-Based Electrolytes Minimize Li Depletion and Pulverization. *Nat. Energy* **2019**, *4* (9), 796–805.

- (24) Cao, X.; Gao, P.; Ren, X.; Zou, L.; Engelhard, M. H.; Matthews, B. E.; Hu, J.; Niu, C.; Liu, D.; Arey, B. W.; et al. Effects of Fluorinated Solvents on Electrolyte Solvation Structures and Electrode/Electrolyte Interphases for Lithium Metal Batteries. *Proc. Natl. Acad. Sci. U. S. A.* **2021**, *118* (9), No. e2020357118.
- (25) Liu, X.; Mariani, A.; Adenusi, H.; Passerini, S. Locally Concentrated Ionic Liquid Electrolytes for Lithium-Metal Batteries. *Angew. Chem., Int. Ed.* **2023**, *62* (17), No. e202219318.
- (26) Liu, X.; Mariani, A.; Diemant, T.; Di Pietro, M. E.; Dong, X.; Mele, A.; Passerini, S. Reinforcing the Electrode/Electrolyte Interphases of Lithium Metal Batteries Employing Locally Concentrated Ionic Liquid Electrolytes. *Adv. Mater.* **2024**, *36* (1), No. 2309062.
- (27) Liu, X.; Mariani, A.; Diemant, T.; Pietro, M. E. Di; Dong, X.; Kuenzel, M.; Mele, A.; Passerini, S. Difluorobenzene-Based Locally Concentrated Ionic Liquid Electrolyte Enabling Stable Cycling of Lithium Metal Batteries with Nickel-Rich Cathode. *Adv. Energy Mater.* **2022**, *12* (25), No. 2200862.
- (28) Weng, W. L.; Chang, Y. C.; Huang, C. P. Densities and Viscosities for Binary Mixtures of Anisole with Pentyl Alcohol Isomers. *J. Chem. Eng. Data* **1999**, *44* (5), 998–1001.
- (29) Beran, M.; Přihoda, J.; Žák, Z.; Černík, M. A New Route to the Syntheses of Alkali Metal Bis(Fluorosulfonyl)Imides: Crystal Structure of  $\text{LiN}(\text{SO}_2\text{F})_2$ . *Polyhedron* **2006**, *25* (6), 1292–1298.
- (30) Liu, X.; Zarrabeitia, M.; Mariani, A.; Gao, X.; Schütz, H. M.; Fang, S.; Bizien, T.; Elia, G. A.; Passerini, S. Enhanced  $\text{Li}^+$  Transport in Ionic Liquid-Based Electrolytes Aided by Fluorinated Ethers for Highly Efficient Lithium Metal Batteries with Improved Rate Capability. *Small Methods* **2021**, *5* (7), No. 2100168.
- (31) Canongia Lopes, J. N.; Costa Gomes, M. F.; Pádua, A. A. H. Nonpolar, Polar, and Associating Solutes in Ionic Liquids. *J. Phys. Chem. B* **2006**, *110* (34), 16816–16818.
- (32) Jiang, H. J.; Fitzgerald, P. A.; Dolan, A.; Atkin, R.; Warr, G. G. Amphiphilic Self-Assembly of Alkanols in Protic Ionic Liquids. *J. Phys. Chem. B* **2014**, *118* (33), 9983–9990.
- (33) Mariani, A.; Dattani, R.; Caminiti, R.; Gontrani, L. Nanoscale Density Fluctuations in Ionic Liquid Binary Mixtures with Non-amphiphilic Compounds: First Experimental Evidence. *J. Phys. Chem. B* **2016**, *120* (40), 10540–10546.
- (34) Mariani, A.; Caminiti, R.; Ramondo, F.; Salvitti, G.; Mocci, F.; Gontrani, L. Inhomogeneity in Ethylammonium Nitrate-Acetonitrile Binary Mixtures: The Highest “Low  $q$  Excess” Reported to Date. *J. Phys. Chem. Lett.* **2017**, *8* (15), 3512–3522.
- (35) Mariani, A.; Engelbrecht, L.; Le Donne, A.; Mocci, F.; Bodo, E.; Passerini, S. Disclosing the Hierarchical Structure of Ionic Liquid Mixtures by Multiscale Computational Methods. In *Theoretical and Computational Approaches to Predicting Ionic Liquid Properties*; Elsevier: 2020; pp 1–67. DOI: 10.1016/B978-0-12-820280-7.00014-0.
- (36) Olschewski, M.; Gustus, R.; Marschewski, M.; Höfft, O.; Endres, F. Spectroscopic Characterization of the Interaction of Lithium with Thin Films of the Ionic Liquid 1-Octyl-3-Methylimidazolium Bis(Trifluoromethylsulfonyl)Amide. *Phys. Chem. Chem. Phys.* **2014**, *16* (47), 25969–25977.
- (37) Olschewski, M.; Gustus, R.; Höfft, O.; Lahiri, A.; Endres, F. Monochromatic X-Ray Photoelectron Spectroscopy Study of Three Different Ionic Liquids in Interaction with Lithium-Decorated Copper Surfaces. *J. Phys. Chem. C* **2017**, *121* (5), 2675–2682.
- (38) Park, K.; Yu, B. C.; Goodenough, J. B.  $\text{Li}_3\text{N}$  as a Cathode Additive for High-Energy-Density Lithium-Ion Batteries. *Adv. Energy Mater.* **2016**, *6* (10), No. 1502534.
- (39) Fan, X.; Chen, L.; Ji, X.; Deng, T.; Hou, S.; Chen, J.; Zheng, J.; Wang, F.; Jiang, J.; Xu, K.; et al. Highly Fluorinated Interphases Enable High-Voltage Li-Metal Batteries. *Chem.* **2018**, *4* (1), 174–185.
- (40) Eshetu, G. G.; Diemant, T.; Hekmatfar, M.; Grugeon, S.; Behm, R. J.; Laruelle, S.; Armand, M.; Passerini, S. Impact of the Electrolyte Salt Anion on the Solid Electrolyte Interphase Formation in Sodium Ion Batteries. *Nano Energy* **2019**, *55*, 327–340.
- (41) Moulder, J. F.; Stickle, W. F.; Sobol, P. E.; Bomben, K. D. *Handbook of X-Ray Photoelectron Spectroscopy*; Perkin-Elmer Corporation, Physical Electronics Division: 1992.
- (42) Chen, J.; Li, Q.; Pollard, T. P.; Fan, X.; Borodin, O.; Wang, C. Electrolyte Design for Li Metal-Free Li Batteries. *Mater. Today* **2020**, *39*, 118–126.
- (43) Miao, Q.; Solan, N.; Hyun, G.; Holoubek, J.; Liu, P. Electrolyte Engineering for Long-Life Li-SPAN Batteries. *ACS Energy Lett.* **2023**, *8* (6), 4818–4830.
- (44) Liu, X.; Diemant, T.; Mariani, A.; Dong, X.; Di Pietro, M. E.; Mele, A.; Passerini, S. Locally Concentrated Ionic Liquid Electrolyte with Partially Solvating Diluent for Lithium/Sulfurized Polyacrylonitrile Batteries. *Adv. Mater.* **2022**, *34* (49), No. 2207155.